Experimental investigations on boundary layer transition over a flat plate with suction and comparison with linear stability theory

Corelli Grappadelli, M.; Asaro, S.; Radespiel, R.; Badrya, C.

DOI
10.1007/s00348-025-04084-z

Publication date
2025

Document Version
Final published version

Published in
Experiments in Fluids

Citation (APA)
Corelli Grappadelli, M., Asaro, S., Radespiel, R., & Badrya, C. (2025). Experimental investigations on boundary layer transition over a flat plate with suction and comparison with linear stability theory. *Experiments in Fluids*, *66*(8), Article 154. https://doi.org/10.1007/s00348-025-04084-z

Important note
To cite this publication, please use the final published version (if applicable).
Please check the document version above.

Experiments in Fluids (2025) 66:154
https://doi.org/10.1007/s00348-025-04084-z

RESEARCH ARTICLE

Experimental investigations on boundary layer transition over a flat plate with suction and comparison with linear stability theory

M. Corelli Grappadelli[1] · S. Asaro[2] · R. Radespiel[1] · C. Badrya[3]

Received: 2 April 2025 / Revised: 14 June 2025 / Accepted: 13 July 2025 / Published online: 30 July 2025

Abstract

Laminar boundary layer suction has significant potential for reducing aircraft drag, thereby diminishing its environmental impact. This study presents wind tunnel experiments conducted on a flat plate to examine the effectiveness of laminar boundary layer suction in delaying the transition and compares the measured data with the e^n method based on linear stability theory (LST). The experiments, performed over a range of freestream velocities from 15 to 50 m/s, comprised infrared thermography, pressure measurements, and hot-wire anemometry. The boundary layer suction is implemented through interchangeable suction boxes mounted on the flat plate, with two types of suction surfaces tested, featuring hole diameters of 120 and 60 µm and a constant porosity of 0.9%. The study examines the influence of various parameters on transition, as the intensity of the suction coefficient, particularly at elevated values, as well as the impact of the micro-holes diameter, the chordwise distribution of the suction velocity and the freestream Reynolds number. A discrepancy between the experimentally measured transition location and the predictions from LST is observed. To identify the origin of this deviation, boundary layer measurements are taken on the porous surface while varying both the suction coefficient and its spatial distribution. A particular flow disturbance near the porous surface, amplified by the suction intensity, is identified, leading to increased velocity fluctuations in the near-wall measurement points. The difference depends on both the suction coefficient and the suction velocity distribution. For this reason, a configuration is investigated in which only the first and last of the four suction chambers are used to aspirate the boundary layer. It is observed that the flow disturbances are significantly reduced, and the boundary layer predictions align more closely with the experimental data.

1 Introduction

Laminar flow control can lead to substantial reduction of the viscous drag thereby increasing the overall efficiency of the aircraft, as described in Beck et al. (2018) and in Braslow (1999). In recent decades, various wind tunnel experiments have demonstrated the advantage of applying laminar boundary layer suction to reduce drag and increase the efficiency of airfoils and nacelles, and most of them are collected in Joslin (1998). As examples, Bobbit et al. (1992) proved a 40% drag reduction on a transonic wing at $M_\infty = 0.81$ and $Re_\infty = 15$ million and Pfenninger (1946) measured a 50% drag reduction on an airfoil at R_∞ =2.4 million.

On a zero pressure gradient subsonic flat-plate, the laminar-to-turbulent transition is dominated by Tollmien–Schlichting instabilities (TSI) Schlichting and Gersten (2017). TSI are streamwise viscous instabilities which are initially generated in the receptivity process close to the leading edge. The TSI can be damped or amplified, and according to Squire's theorem are two-dimensional for incompressible flow Squire (1933). The initial growth of these waves may be described by Fourier modes and can be solved by linear stability equation based on the Orr–Sommerfeld equation. For high enough amplitude of TS-waves, three-dimensional waves develop leading to turbulent spots which finally cause

✉ M. Corelli Grappadelli
m.grappadelli@tu-bs.de

S. Asaro
S.Asaro@tudelft.ne

R. Radespiel
rolf.radespiel@tu-bs.de

C. Badrya
cbadrya@ucdavis.edu

[1] Institut of Fluid Mechanics, TU Braunschweig, Hermann Blenk Strasse 38, Braunschweig 38108, Germany

[2] Faculty of Aerospace Engineering, TU Delft, Kluyverweg 1, Delft 2629HS, The Netherlands

[3] Aerospace Engineering, University of California, One Shields Avenue, Davis, CA 95616, USA

the transition to fully turbulent flow. Boundary layer suction enhances flow stability by reducing the boundary layer thickness and modifying the velocity profile, effectively delaying the growth of TS instabilities and the onset of transition Schlichting and Gersten (2017). An experiment that applied a laminar flow control strategy to an aircraft nacelle was conducted by Gregory and Walker (1957). By implementing suction in two specific sections of the nacelle, the transition point of the laminar flow was significantly extended, from 37 to 82% x/c.

Measurement of the velocity profiles with a hot-wire anemometer has shown that the suction is more efficient in the region where disturbances are still small in amplitude Reynolds and Saric (1985), confirming numerical predictions performed by Reed and Nayfeht (1982). Experiments employing flush mounted microphones to determine the transition region with two different suction panels have shown good agreement with the LST predictions Hackenberg et al. (1995). Another experiment on a flat plate shows that LST slightly overestimates the decay factor when compared to experiments, while the corresponding amplitude and disturbance phase were in good agreement Fransson and Alfredsson (2003).

The presence of defects as wires, forward-facing steps, and gaps on the flat plate with suction affects the transition location only above a critical value that can be related to the boundary layer displacement thickness Methel et al. (2015) and Heintz and Scholz (2023a).

The intensity of laminar boundary layer suction is characterized by the total suction coefficient:

$$c_Q = \frac{Q}{S_{ref} U_\infty} = \frac{1}{c} \oint_S \frac{v_0}{U_\infty} \mathrm{d}s \tag{1}$$

where S_{ref} denotes the area of the suction box and v_0 represents the homogeneous suction velocity through the porous medium, following the definitions provided in Pfenninger (1946) and Iglisch (1944). The latter reference provides detailed guidelines for calculating the boundary layer under conditions of uniform suction, and in particular, it introduces and analytically supports the concept of the asymptotic boundary layer. Significant efforts in the 1950 s and 1960 s were dedicated to investigating the destabilizing interaction between aspirated streamtubes and the boundary layer. The most widely referenced stability criteria remains that of Goldsmith (1957) for a single row of suction holes. With the suction holes positioned closely together, the streamwise disturbance vortices generated by suction are confined to the slowest region of the boundary layer. Under these conditions, the disturbance vortices caused by the suction holes remain weak enough for viscous forces to dominate over pressure and inertia forces, leading to their fast dissipation. This scenario is identified in Goldsmith's parametric map (well described in Pfenninger and Syberg (1974)), as the condition in which the ratio between α (spacing between adjacent rows of holes) and h (the height of the streamtube suctioned through the hole) is extremely low. The very same parametric map is analyzed years later with the gained experience in flight test, in Hefner and Sabo (1987). Particularly, it is hypothesized that the transition shifts to higher Re_k (Reynolds number based on the suctioning holes diameter) in the case of suction through multiple lines of holes, demonstrating a beneficial effect in stability, which was not discussed in detail in the first version of the method. In general, the focus moved toward the interaction of vortices and the possibility of predicting their behavior using numerical techniques (LST and Direct Numerical Simulations, DNS as in the work of Macmanus and Eaton (1996), Macmanus and Eaton (1998)) already at the design stage. This is especially critical for leading-edge suction, where the boundary layer thickness poses significant challenges relative to the achievable hole dimensions, and for the adverse interaction of vortices with crossflow instability along the spanwise direction, studied in the DNS work from Messing and Kloker (2010).

Recently, increased research attention has been directed toward the origin of an additional disturbing interaction between the porous surface (including the entire suction volume) and the external boundary layer itself. This phenomenon was observed in flight experiments Schrauf (2015) through comparisons with LST, and its existence was already known as reported in Pfenninger (1977). Consequently, Tilton and Cortelezzi (2015) analyzed the system using LST and found that the maximum level of stabilization achievable is considerably lower than that predicted by classical theory. Furthermore, Rouviere et al. (2022) conducted experiments on a flat plate with a porous surface to obtain data useful to implement a correction for the linear stability theory. Good agreement between experimental and numerical results was found for low impedance values. Finally, Von Soldenhoff and Lüdeke (2024) reconfirmed these findings through DNS performed over a discretely slotted surface modeling also the underlying suction chamber geometry.

The present study examines the effects on the transition caused by the characteristics of porous surfaces, the suction coefficient (with a particular emphasis on strong suction coefficients $> 10^{-3}$), and the distribution of the suction velocity along the aerodynamic chord. In the work by Sudhi et al. (2021), the importance of high suction coefficients was emphasized when transition needs to be delayed in regions subjected to a significant adverse pressure gradient, a finding that was further confirmed during the wind tunnel experiment described in Corelli Grappadelli et al. (2022). Wind tunnel experiments conducted at several Reynolds numbers investigate the influence on the laminar boundary layer profiles of suction box hole diameters of 60 µm and 120 µm, suction coefficients up to $5{\times}10^{-3}$, and the differences between a

uniform and non-uniform suction velocity profiles along the chord. The study aims to assess their cumulative effects by measuring the laminar-to-turbulent transition position. Additionally, the individual effects are determined by measuring the velocity profiles with a focus on isolating the influence of each factor. First the porosity of the holes, then the intensity of the suction, and lastly the distribution of suction along the chord.

2 Experimental setup

2.1 Flat plate model and testing conditions

The tests are conducted in the low-speed wind tunnel MUB (Modell-Unterschall-Windkanal Braunschweig, MUB) at Technische Universität Braunschweig. The wind tunnel is a Göttingen-type with a closed test section of 1.3 m × 1.3 m × 6 m. A heat exchanger in the settling chamber is used to stabilize the temperature of the flow. Petzold and Radespiel (2015) reported a turbulence intensity level of 0.17 % at 50 m s^{-1}, measured at three different positions within the test section using a high-pass filter at 20 Hz and a sampling frequency of 100 kHz with an observation time of 10 s. Similar values were obtained in the present study at the geometric center of the test section, where the turbulence intensity ranges from 0.05 % at 15 m s^{-1} to 0.18 % at 50 m s^{-1}, corresponding to the minimum and maximum freestream velocities tested, when using the same acquisition parameters.

Figure 1a shows the flat plate model inside the wind tunnel. The flat plate has a chord $c = 4.06$ m and a span $b = 1.3$ m. In this study, since the length of the laminar regime extends from less than one meter to over two and a half meters, a unit Reynolds number is used ($L_{\text{ref}} = 1$ m), resulting in a range of $Re = 0.9$–3.0×10^6.

The thickness of the flat plate directly influences the boundary layer stability. A thinner plate facilitates the establishment of a zero pressure gradient (lower acceleration); however, it must also accommodate the suction system. A thickness-to-chord ratio of $t/c = 1.73\%$ is selected based on predictions from Xfoil Drela (1989), coupled with a linear stability analysis performed with COCO-LILO Schrauf (1998); Schrauf and Horstmann (2000). For comparison, previous studies have employed flat plate thickness ratios of 2% Helm et al. (2024), 2.48% Methel et al. (2015), and 4.28% Heintz and Scholz (2023a).

A schematic of the flat plate is shown in Fig. 1b. The flat plate is comprised of several components, a leading edge, an interchangeable suction panel, two carbon fiber plates and the trailing edge flap. The characteristics and design of the leading edge and of the suction panel are discussed in detail in Sects. 2.1.1 and 2.1.2, respectively.

Further downstream of the suction panel, the model consists of two composite-based flat plates, each measuring 1.15 × 1.3 m. These plates are specifically designed for infrared (IR) thermography measurements. Further details on the characteristics of the plates and the measurement methodology are provided in Sects. 2.1.3 and 2.2.3, respectively.

2.1.1 Leading edge design

A critical part of the overall design is the flat plate leading edge, as it directly influences the starting and development of instabilities. To achieve precise control over the leading edge shape, a Bezier curve generator was coupled with Xfoil Drela (1989) for computing the pressure distributions. The

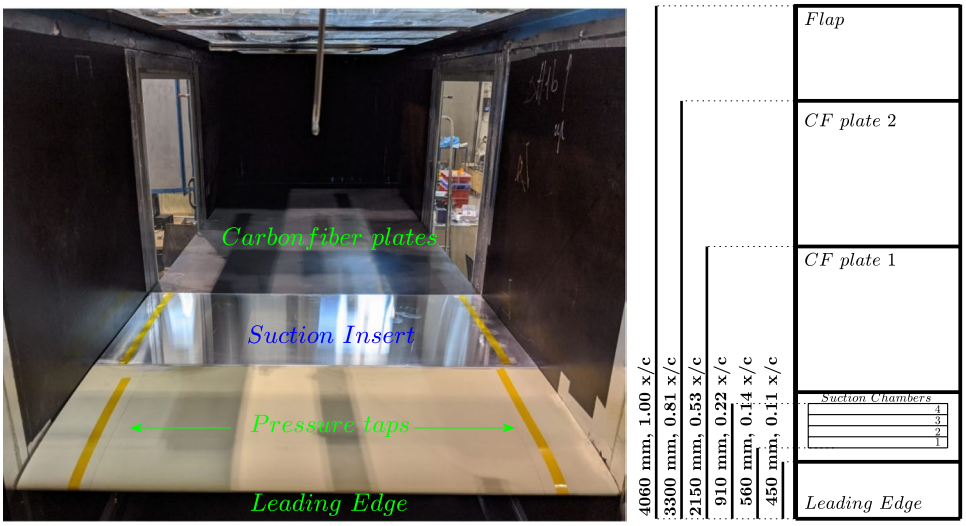

(a) Flat plate model inside the wind tunnel. (b) General dimensions.

Fig. 1 Experimental setup, general dimensions and components

design process was conducted by analyzing the growth of the N-factor through the COCO-LILO linear stability tool, described in Schrauf (2006), applied to the pressure distributions calculated by Xfoil. A leading edge was designed to delay the growth of the critical amplification factor N along the chord. Particular emphasis was placed on achieving a low-suction peak to delay the onset of Tollmien–Schlichting (TS) instabilities.

This approach allowed for meticulous manipulation of the leading edge geometry by adjusting the coordinates of six control points, reported in Eq. 2. The usable length of the CNC milling machine's worktable was fully leveraged, establishing a maximum allowable length for the leading edge at 0.45 m × 1.3 m.

Employing a symmetrical solution and aiming at minimizing the thickness to the construction limit of 70 mm were the driving criteria in order to obtain a stable and weak acceleration on both sides of the flat plate. Further details on the pressure distribution and related critical amplification factor are explained in Sect. 2.2.4.

$$\begin{cases} B(t) = (1-t)^5 \cdot P_0 + 5t \cdot (1-t)^4 \cdot P_1 + 10t^2 \cdot (1-t)^3 \cdot P_2 + \\ \qquad + 10t^3 \cdot (1-t)^2 \cdot P_3 + 5t^4 \cdot (1-t) \cdot P_4 + t^5 P_5 \\ P_0 = [450, 35] \qquad P_1 = [259.77, 34.3] \qquad P_2 = [-175, 35] \\ P_3 = [-175, -35] \qquad P_4 = [259.77, -34.3] \qquad P_5 = [450, -35] \end{cases} \tag{2}$$

2.1.2 Suction box design

The boundary layer suction is exerted by a suction box, displayed in Fig. 2a, consisting of four independent suction chambers, one of which is depicted in Fig. 2b. This layout has been specifically designed to generate the suction velocity as uniformly as possible across the entire opening of the suction box, spanning over 1100 mm while aspirating the air from only one side of the model, similarly to what has been done in Gregory and Walker (1955).

The suction box is constructed using three different interchangeable layers, which are visible in Fig. 2a. The top layer is the porous skin, which is a stainless steel sheet, 0.8 mm thick, featuring holes measuring either 120 µm or 60 µm, with a porosity of 0.9%. Further details on the same porous material can be found in Prasannakumar et al. (2022). This layer is in direct contact with the boundary layer of the flat plate. Beneath, 24.8 mm lower, there is a 1 mm thick metal sheet with 5 slit holes per chamber, measuring 185 mm × 0.8 mm aligned along the y-axis of the model. The induced pressure loss is introduced to ensure a homogeneous flow beneath the porous surface through all the span and chord, and to prevent any flow recirculation within the first layer. Below there is a secondary chamber, which encloses a volume with a ramp-shaped bottom surface inclined at 1.74°. The purpose of this ramp is to account for viscous losses by sucking the air from only one side of the suction box for the entire span of the flat plate.

The air is drawn via a high-pressure side channel ventilator with a maximum power of 5.5 kW that can produce

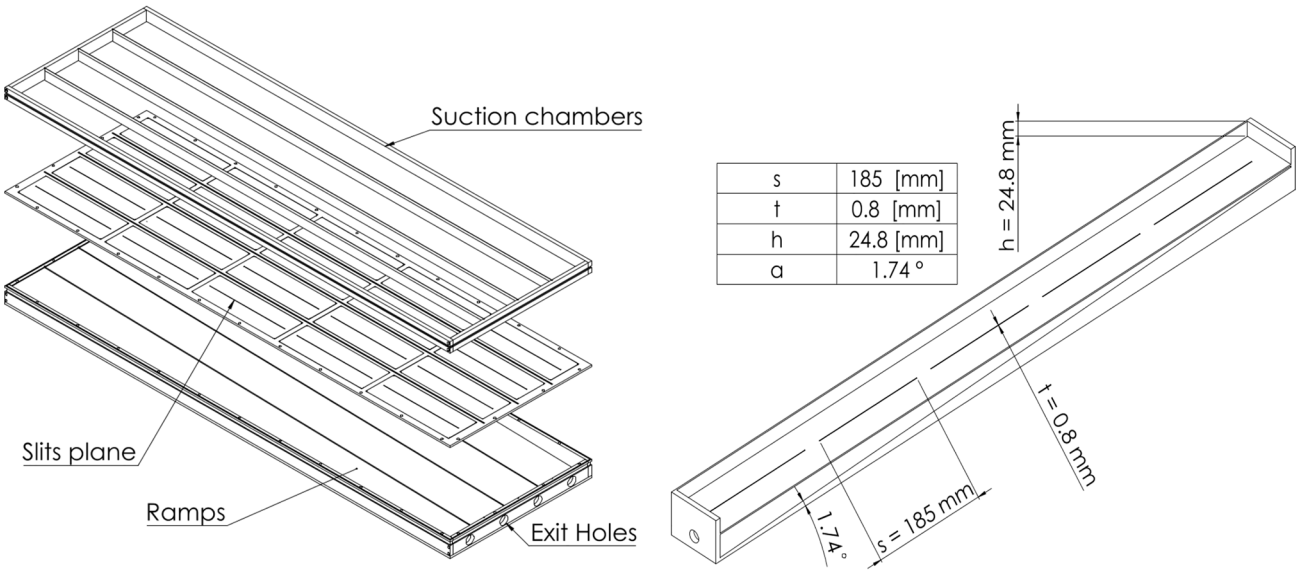

(a) Suction box exploded view. (b) One of the four suction chambers.

Fig. 2 Suction box general layout and dimensions

a pressure difference of 52.5 kPa at a volume flow of up to 165 m^3/h. The power requirement is primarily due to the installed flow losses in the fluidic system, which serve to dampen unwanted flow rate oscillations characteristic of these side-channel blowers. The suction rates of each chamber are individually controlled using 4 proportional valves Bürkert-3285, with 24-Volt stepper motors, which are remotely controlled and adjusted to achieve the desired pressure loss through the porous skin. The flow rate is also controlled in real-time using a Höntzsch model Ta Di 27.2 GE60 and three Testo 6441 (whose details are provided in Sect. 2.2.2) flow meters, whose signals are not recorded but are used only to regulate the airflow rates.

Pressure taps offer a reliable means of measuring the suction coefficient by sampling the static pressure 3 mm beneath the porous skin, within the four suction chambers. The uniformity of the suction velocity is monitored through these pressure taps, which are positioned along the lateral walls of each chamber, one per side for the first three chambers, and three per side for the last chamber.

2.1.3 Composite plates

Two flat plates, each measuring 1150 × 1295 mm, were fabricated and mounted sequentially in the test section. The plates consist of a composite sandwich structure with an embedded graphite layer. When connected to a 300 W power source, this layer heats the outer surface, while the inner surface is thermally insulated with Rohacell and a thicker fiberglass layer. This method, previously employed in Petzold and Radespiel (2015), leverages the differing thermal convection properties of laminar and turbulent flows to identify the transition location, which appears as a boundary between a warmer laminar region and a cooler turbulent region, with a temperature difference of approximately 2.5°C.

2.2 Measurement techniques

Several measurement techniques are employed, in order to obtain the pressure distribution (Sect. 2.2.1), the transition location (Sect. 2.2.3) and the boundary layer profiles (Sect. 2.2.5) on the flat plate, as a function of the aspirated mass flow (Sect. 2.2.2).

2.2.1 Pressure measurements

The pressure distribution along the flat plate in the streamwise direction is measured with two lines of pressure taps placed at $0.17b$ and at $0.83b$. Each side features a total of 38 pressure taps distributed as in Fig. 3a, with a diameter of 0.3 mm. The pressure taps do not influence the infrared measurements because their region of influence is located outside of the camera Field of View (FOV)(Sect. 2.2.3). The pressure is measured with two pressure scanners, with 32 and 64 channels, where each channel features a differential pressure transducer with individual offset and thermal compensation (range = ±1 Psi). The precision is limited to ±0.05% of 1 Psi, which corresponds roughly at ±3.5 Pa for the full range of the scale. For each run set, the steady measurements are obtained by averaging 2500 samples for each

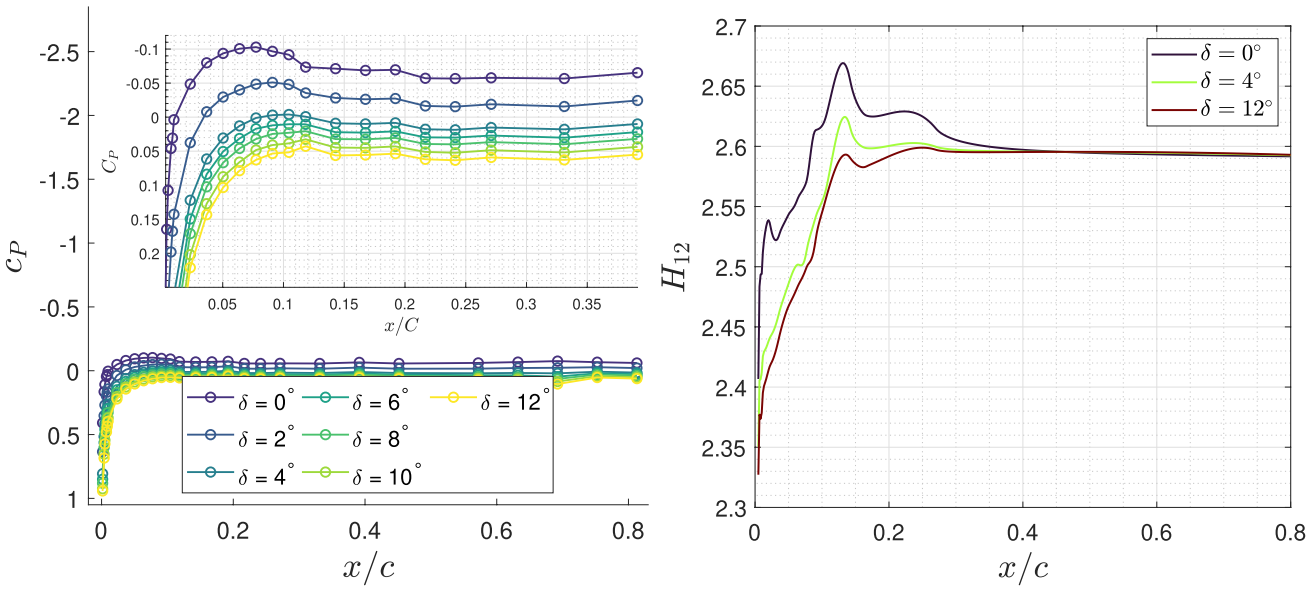

(a) Pressure coefficient distribution.

(b) Shape factor distribution.

Fig. 3 Pressure distributions for different flap angles and resulting shape factor with COCO

pressure tap, with a frequency of 20 Hz. The uncertainty in the measured pressure coefficient c_P is presented in Sect. 2.4.

Additional pressure taps are used to measure the pressure inside the suction box as explained in Sect. 2.1.2. All the pressure taps used in this experiment, including the ones inside the suction box, are made from stainless steel tubes with an outer diameter of 1 mm and an inner bore of 0.3 mm. In the case of the leading edge, since it is milled from a solid block of high-density plastic, each tube is inserted into a plastic cavity drilled with a 0.3 mm bit from the outside into the center of the metal tube.

The pressure distribution along the flat plate is regulated by the trailing edge flap. The suction peak on the leading edge can be controlled, as shown in Fig. 3a, when the flap angle δ is increased from 0° to 12° upward. In particular, the length and behavior of the Zero Pressure Gradient (ZPG) zone remains approximately constant, becoming positive and continuing to grow with increasing deflection angles. A positive angle of 4° yields the pressure distribution closest to zero without resulting in a large suction peak; therefore, it was chosen for testing. These experimentally measured pressure distributions are subsequently employed as inputs for the boundary layer code COCO Schrauf (1998) and the linear stability code LILO Schrauf (2006) for the LST analysis. Figure 3b shows the shape factor computed with COCO, highlighting the extent to which the influence of the nonzero pressure coefficient near the leading edge persists downstream. As observed, shortly after the minimum in the c_p distribution, H_{12} stabilizes to a nearly constant value along the rest of the flat plate.

2.2.2 Suction velocity measurements

A thermal flow meter was employed to generate the data shown in Fig. 4, establishing the relation between the suction velocity and the pressure loss through the porous skin. The flow meter is a Höntzsch model Ta Di 27.2 GE60, with a measuring range of 7 to 2092 L min^{-1} and a measurement uncertainty of 2% of the actual measured value across the entire measured range. This flow meter was used to produce the curves shown in Fig. 4 for all four suction chambers.

This flow meter was then assigned to one of the four suction lines and placed in parallel with three Testo 6441 flowmeters, which have a greater uncertainty (±3.3%).

As discussed in the following section, relative to uncertainties in Sect. 2.4, the pressure losses below the porous surface were measured to control the suction velocity.

2.2.3 Infrared thermography

The transition from laminar to turbulent flow on the flat plate is measured using an infrared (IR) camera, the Infratec Image IR 8320, equipped with a 25 mm focal

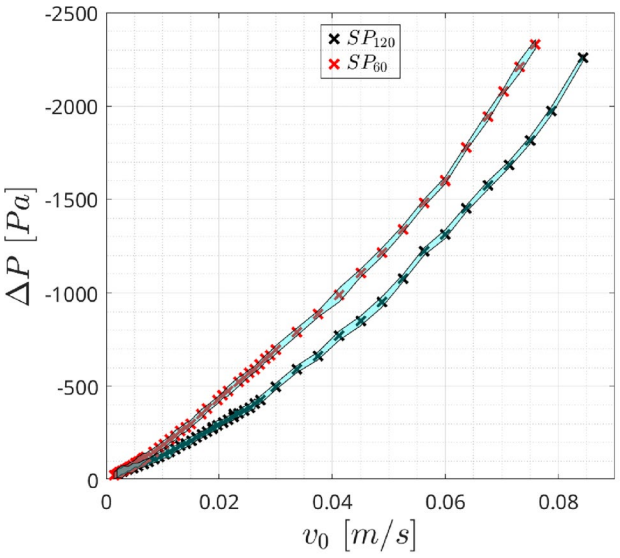

Fig. 4 Pressure losses as a function of the homogeneous suction velocity

length lens and a resolution of 640 × 512 detector elements. The recordings have an observation time of 10 s at 100 Hz, resulting in a total of 1000 samples. The camera is mounted above the wind tunnel test section, measuring the flat plate through a small circular opening in the ceiling. Figure5 shows an example of the raw IR measurements. To ensure stable airflow and minimize interference with the test section, the camera is housed in a sealed box. As visible from Fig. 5 the camera is positioned at an angle rather than perpendicularly to capture a larger surface area. Consequently, the raw images are post-processed to correct for inclination and lens distortion, as displayed in Fig. 6a. The IR field of view extends from 0.268c to 0.691c chordwise and only the central portion is considered from 0.4b to 0.6b spanwise.

A post-processed example is shown in Fig. 6c, displaying temperature contours (°C) on the flat plate, with three lines indicating the beginning, center, and end of the transition process. Various methods exist in the literature to identify the transition point, such as those proposed by Simon et al. (2016), Gauffre (1988), and Petzold and Radespiel (2015). In this work, the transition is determined using the method also adopted in Petzold (2014), where the tangent at the point of minimum gradient $\frac{\partial T}{\partial x}$ intersects the constant temperature lines corresponding to the maximum and minimum temperatures near the transition, marking the onset and completion of the transition process, respectively. The transition locations X_{tr} are referenced within a coordinate system where the origin corresponds to the onset of instabilities, near the peak of the pressure coefficient (c_p) distribution along the leading edge of the flat plate. The minimum is evident in

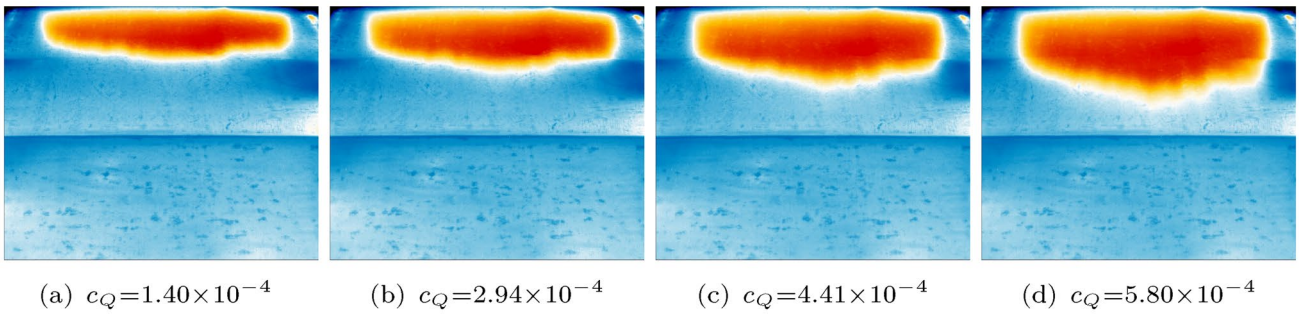

Fig. 5 Transition progression with increasing c_Q, Re=1.51×10^6 (flow from top to bottom)

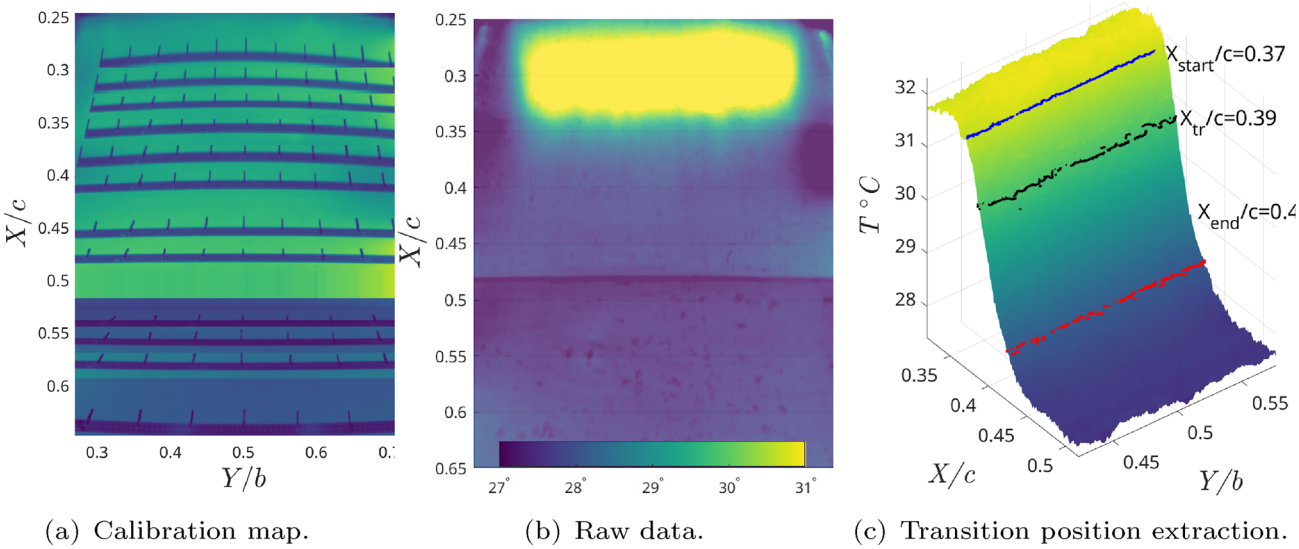

Fig. 6 Processing of the infrared measurements

Fig. 3a, where, for a flap angle of 4 degrees and a test section velocity of 30 m/s, it is located at approximately x/c=0.1.

2.2.4 Critical amplification factor computation

Linear stability analyses are conducted for computing the amplification factor (N) growth and determining the critical N-factors (N_{crit}) for different operating conditions, in particular changes of c_Q. The pressure coefficient distribution (Sect. 2.2.1) together with the geometry of the flat plate, the suction velocity profile, and the flow conditions are the inputs for the COCO code Schrauf (1998). The code enables the calculation of boundary layer properties, such as the boundary layer velocity and temperature profiles, and their first two derivatives for specified chordwise and wall-normal stations. The results obtained from the COCO code serve as input for a linear stability analysis conducted with the LILO code Schrauf (2006), which is based on the full e^N method Van Ingen (2008). The primary output of the linear stability analysis is the N-factor envelope, delineating the maximum amplification ratio along the chordwise direction of the TS instabilities. The critical N-factor of the experiment is then computed by intersecting the amplification rate curve from the linear stability theory with the transition position, determined with the infrared camera (Sect. 2.2.3).

2.2.5 Hot-wire measurements

The boundary layer velocity profiles are measured with a hot-wire anemometer (HWA) at 16 different location along the chord of the flat plate, and with different c_Q. The hot wire is the Dantec 55P11 straight-type, connected with the Streamline-Pro Constant Temperature Anemometry (CTA) system. The Wheatstone bridge is operated with a fixed overheat ratio of 0.95 to keep the negative effects of wall proximity Bruun (1995) low. The hot wire is calibrated inside the wind tunnel in the vicinity of the Prandtl tube used to control

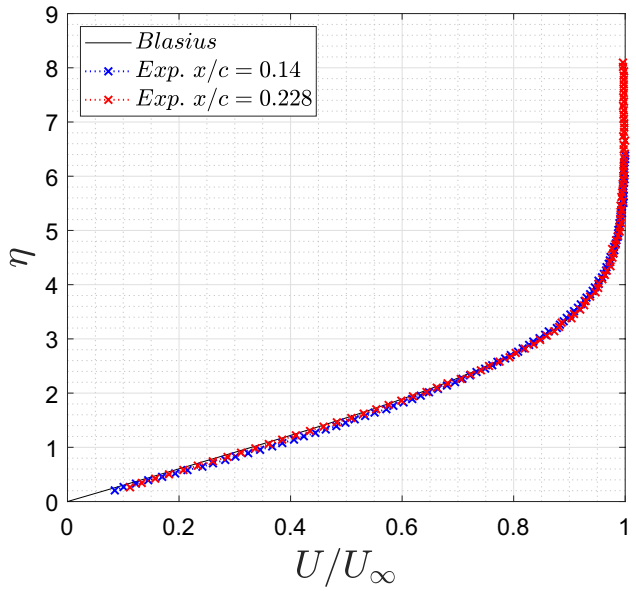

Fig. 7 Comparison between Blasius velocity profile and the experimental data at different chord locations, right before and after the porous skin, c_Q=0

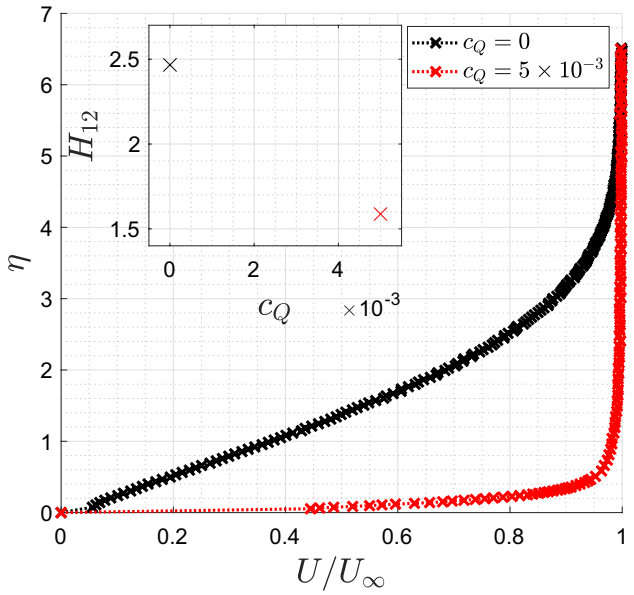

Fig. 8 Comparison of two velocity profiles for $c_Q = 0$ and $c_Q = 5 \times 10^{-3}$ at x/c = 0.225

the wind tunnel speed, and it is located at the center of the test section and upstream of the flat plate.

The observation time was 2.5 s per sample with an acquisition frequency of 40 kHz. For few positions where higher resolution near the wall was required, the observation time was increased to 5 s with an acquisition frequency of 20 kHz.

Figure7 compares two boundary layers measured into two different chordwise measurement points x/c = 0.14 and 0.225, before and after the suction panel, with the Blasius boundary layer. The experimental data are closely matching the theory proving the accuracy of the measurement system. The initial coordinate value for the calculation of the similarity variable η, is considered to be the start of the adverse pressure gradient after the peak of the c_P distribution at x/c= 0.1. The hot wire is mounted on a Physik Instrumente VT-80 linear stage, featuring a maximum travel range of 50 mm. Its real-time position is recorded via an incremental rotary encoder attached to the stage's drive shaft. The hot wire is supported by an 8 mm diameter carbon fiber rod, which is directly connected to the motorized stage. This rod is housed within a 20 mm × 8 mm steel pipe, with two axial recirculating ball bearings ensuring smooth motion between the rod and the pipe. To suppress vortex shedding, the steel pipe is enclosed with an aerodynamic cover.

Figure 8 presents the boundary layer with the highest c_Q compared to the case without suction, at the final measurement location on the porous skin. As discussed in the results Sect. 3.2.2, this position is the most critical for determining the shape factor due to the substantial removal of the boundary layer.

Furthermore, as reported in detail by Iglisch (1944) the near-wall part of the boundary layer is curved. As regards to the height of the first measurement point from the wall, a consideration is made from the trend of the momentum thickness distribution within the boundary layer. The height from the wall of the first point in Fig. 8 is amounting to 50 µm ± 10 µm from the wall, where the uncertainty is given by the motorized linear stage operated in bi-directional mode. Apart from the first point all the remaining points have an uncertainty of ± 0.8 µm as the motor is operated in unidirectional mode. This measurement is taken mainly for checking the approximation introduced when computing the shape factor for high suction coefficient, using a digital dial gauge with an accuracy of ± 1 µm. At such distances from the wall, it is impractical to take measurements due to both technical complexity, which slows down the wind tunnel acquisition process (additional calibrations are needed if the probe touches the surface), and due to the wall's thermal interference effect Bruun (1995). This effect is particularly evident in the reference case without suction, whereas it is mitigated when BLS is applied, as the increased wall heat flux and local flow velocity reduce the influence of wall temperature on the probe response. The first point distance is chosen by observing the momentum thickness distribution. The aim is to measure the maximum value of such distribution to better interpolate the points up to the origin. For the measurements, interpolation of the data at the wall is justified

only in cases with suction coefficients exceeding $c_Q = 3 \times 10^{-3}$, thus avoiding distance from the wall below 200 µm. At this distance from the wall, the measurements are less affected by thermal interactions with the wall but they still provide reliable values of the shape factor, since the maximum in the momentum distribution is well measured.

2.3 Roughness measurements

The surface roughness of the porous surfaces was measured using high-precision mechanical profilometers, specifically the Hommel Waveline W5 model. This roughness measuring device is certified as Class 1 according to the measurement instrument standards of DIN 4772.

The instrument was applied to the porous surfaces SP_{60} and SP_{120} to measure roughness at fifty different points, which were then averaged to obtain the results reported in Table 1. The roughness data of these two porous surfaces are also compared with the non-porous surface SP_0 surface utilized in the test. Additionally, for having a comparison the roughness is also calculated on a cast aluminum plate that has been sanded using P100, P400, P800, and P2000 abrasive papers.

In Table 1, R_a represents the arithmetical mean deviation from the reference plane, R_z denotes the mean maximum height, and R_t indicates the maximum height measured, all according to the DIN EN ISO 4287 standard. Compared to the rest of the flat plate elements and their interconnecting gaps, which were sanded with P2000 grit, the porous surfaces are at least one order of magnitude rougher. The roughest surface, SP_{60}, is nearly three times rougher than SP_{120} due to the more intensive laser drilling process, reduced hole spacing, and increased hole count. Further sanding of the porous surfaces after the laser drilling process was avoided to prevent clogging the holes, which would hinder achieving a uniform suction condition.

Steps between the components of the wind tunnel model can significantly impact the repeatability of laminar flow experiments since as already explained in works by Methel et al. (2015), Heintz and Scholz (2023a) and Zhao and Dong (2020), as laminar flows are highly susceptible to steps and gaps. For this reason, concentric differential screws were installed every 100 mm along all junctions between components (leading edge, suction panel, and carbon fiber plates) to precisely adjust the step height within ±50 µm, verified using a digital dial gauge. Once adjusted, the steps were covered with fairing compound and sanded up to a sandpaper grit value of 2000 with the aid of water. Given the extended wind tunnel testing duration, this compound was checked daily due to its tendency to degrade under loads and vibrations. The most stringent step condition (Backward Facing Step, BFS) can be estimated with the criterion devised by Nenni and Gluyas (1966)-recently employed also in the work of Heintz and Scholz (2023a). For the analyzed wind tunnel velocities, the critical step values are ranging from 900 µm at 15 m/s to approximately 300 µm at 50 m/s. Hence, the maximum step measured of 50 µm should not affect the results.

Regarding the statistics on the hole dimensions, conicity and pattern, the reader is referred to the work of Prasannakumar et al. (2022), where the same porous material as in this experiment is used.

2.4 Uncertainty

Table 2 presents the systematic $b_{\overline{X}}$ and random $s_{\overline{X}}$ uncertainties, with an entry provided for each measured technique employed in the experiment. The calculation of random uncertainty is performed by analyzing the standard deviation of the quantity X measured in conjunction with the number of samples collected. Systematic uncertainties are determined through the specification sheets provided by the manufacturers of the measurement instruments and the calibration curves. The values reported in the table reflect the most severe conditions tested, specifically with the flow in the test section set at 50 m/s, to represent the worst-case measurement scenario. The nomenclature proposed by ASME (2006) is followed throughout this work.

The combined uncertainties, represented in this study with shaded areas in all the graphs, are calculated using

Table 2 Random ($s_{\overline{X}}$) and systematic ($b_{\overline{X}}$) standard uncertainty for applied measurement systems

Measuring tool	$s_{\overline{X}}/\overline{X}$, %	$b_{\overline{X}}/\overline{X}$, %
Mass flow meters, Hontzsch	–	2
Mass flow meters, Testo 6441	–	3.2
Pressure transducers	3.3×10^{-7}	1.7×10^{-3}
Infrared measurements	5	1
Hot wire (calibration)	5×10^{-3}	0.1

Table 1 Roughness characteristics for SP_{120} and SP_{60}

	P100	P400	P800	P2000	SP_0	SP_{120}	SP_{60}
R_a	1.40 µm	0.46 µm	0.26 µm	0.11 µm	0.24 µm	1.31 µm	3.12 µm
R_z	10.58 µm	3.84 µm	2.69 µm	1.18 µm	1.80 µm	18.12 µm	39.98 µm
R_t	14.21 µm	6.15 µm	4.16 µm	1.61 µm	2.90 µm	50.77 µm	71.85 µm

the formula $\delta X = \sqrt{s_{\bar{X}}^2 + b_{\bar{X}}^2}$ and expanded to a 95% confidence level.

3 Results

The influence of the suction coefficient c_Q on the transition location is analyzed in Sect. 3.1, considering a range of unitary Reynolds numbers $Re = 1.8 - 3 \times 10^6$, which correspond to freestream velocities between 30 and 50 m/s. The analysis is conducted for two porous panels featuring hole diameters of 60 µm and 120 µm. The behavior of the critical amplification factor N_{crit} under different suction conditions is investigated using LST and compared with experimental data.

Further comparison between the experimental data and the numerical predictions is made in Sect. 3.2 where the evolution of the boundary layer over the porous surface is examined using hot-wire anemometry for various values of c_Q. These tests are conducted at $Re = 0.9 \times 10^6$ ($U_\infty = 15\,\text{m s}^{-1}$) on the panel with 120 µm diameter holes, as this panel has demonstrated superior performance in previous investigations. The study first examines the effects of permeability, surface roughness, and impedance on the stability of the laminar boundary layer in the absence of suction (Sect. 3.2.1). Subsequently, boundary layer suction is activated, and the effect of increasing the suction coefficient is examined up to relatively high values in Sect. 3.2.2. In conclusion, Sect. 3.2.3 examines a discontinuous suction distribution using chambers 1 and 4, highlighting the effects of spatial variations in boundary layer suction and their consistency with numerical predictions.

3.1 Transition and critical amplification factor

The transition positions from laminar to turbulent boundary layer are analyzed employing the infrared camera as outlined in Sect. 2.2.3.

Two different porous surfaces are tested with hole diameters of 60 and 120 µm, SP_{60} and SP_{120}, respectively, and with the same porosity level of 0.9%. Further details on the porous plates can be found in Prasannakumar et al. (2022).

Figure 9 compares the laminar boundary layer extension as a function of the wind tunnel velocity expressed via the Reynolds number Re (which considers a unitary reference length), for SP_{60}, SP_{120}, and SP_0, i.e., a metallic panel without holes. At wind tunnel velocity $U_\infty > 35$ m/s, corresponding to Re=2.12×10^6 the transition occurs on the metallic suction panel where it is not possible to measure with the infrared camera due to the metal's emissivity. The

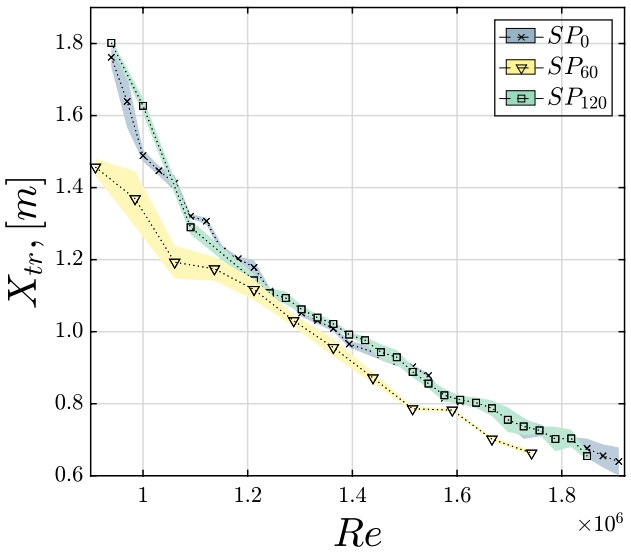

Fig. 9 Natural X_{tr} for SP_0, SP_{60} and SP_{120}

difference of the natural transition location between the case with and without suction box are related to small disturbances introduced by the installation of the suction box itself. Overall, the discrepancies in the transition location between SP_0 and SP_{120} are minimal, especially at higher Re, whereas SP_{60} appears to be slightly lower, particularly at lower velocities.

Smaller holes are generally associated with lower disturbances in the boundary layer due to the reduced permeability of the panel, Tilton and Cortelezzi (2015). The different trend here observed is primarily driven by the panel's roughness, which is approximately three times higher than that of SP_{120}, as it is reported in Sect. 2.3.

As discussed in detail in Sect. 3.2.1 for a test case at $Re = 0.9 \times 10^6$, such effects are present but exert only a minor influence on transition. This is evident from the direct comparison between the non-porous configuration SP_0 and SP_{120}, which, due to its larger hole diameter, would be expected to exhibit the most pronounced permeability effects.

The suction coefficient c_Q exerts a direct influence on the transition location as visible in Fig. 10. The graph features the transition position as a function of c_Q (for both SP_{60} and SP_{120}), for several unitary Reynolds number Re. The transition location, X_{tr}, is evaluated starting from $x/c = 0.1$, corresponding to the onset of TSI amplification. This reference point is chosen due to the significant sensitivity of the transition length to variations in c_Q, thereby enabling a more consistent and meaningful comparison in terms of unit Reynolds number. For all the Reynolds numbers tested, increasing c_Q leads to a shift of the transition location downstream, and the relation appears to be linear for low suction rates. Subsequently, the transition appears to converge to an

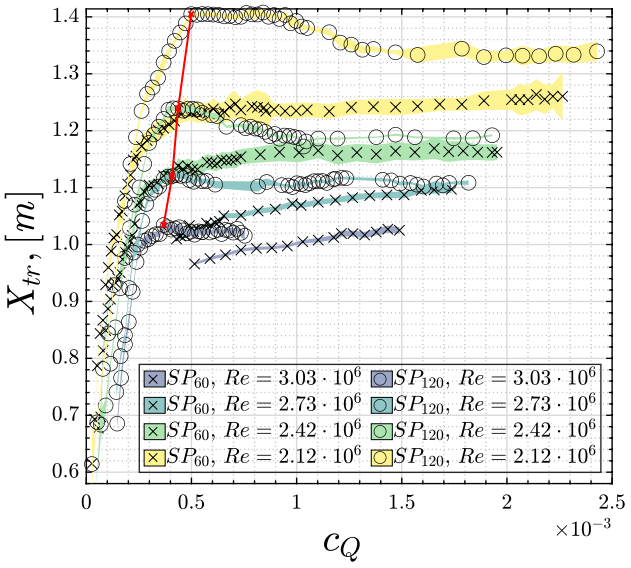

Fig. 10 X_{tr} as a function of c_Q for SP_{120} and SP_{60}

asymptote, indicating that beyond a certain suction coefficient, no additional benefit is gained.

For the tested Reynolds numbers and c_Q, the SP_{120} surface always outperforms the SP_{60}. The linear region of SP_{120} ends close to $c_Q = 0.5{\times}10^{-4}$, and such upper limit of useful suction coefficient decreases with increasing Reynolds numbers, going from 5×10^{-4} for Re = $2.1{\times}10^6$ to $3.7{\times}10^{-4}$ for Re = $3.0{\times}10^6$, as highlighted through a red line in Fig. 10.

Only for the SP_{120} surface, at the lower Reynolds number tested and at the higher c_Q cases, the transition location moves gradually upstream with increased c_Q. Hence, the effect here observed is different to the often called, "oversuction" or "strong suction" effect, first observed and characterized by Goldsmith (1957) and subsequently in several works by Pfenninger-most notably in Pfenninger and Syberg (1974) and Pfenninger (1977), which provide the methodological guidelines.

In the case of oversuction, as predicted by Goldsmith's criterion, the transition to a turbulent regime would be triggered immediately downstream of the porous surface, or as more recently reported by Macmanus and Eaton (2000), at a distance corresponding to 110 diameters. While the vortices described in Goldsmith's work can sometimes exhibit both unfavorable and, more rarely, favorable interference effects, in the present experiments they do not appear to be responsible for the regression of transition.

In conclusion, the observed transition mechanism is not associated with the super-position of turbulent vortices.

The effect, so far described, does not occur with SP_{60}, where the transition always gradually increases with c_Q. From the curves trend, it can be deduced that the performance gap between the SP_{60} and the SP_{120} reduces as the Reynolds number increases, and it almost disappears for the highest tested c_Q values.

As explained in Sect. 2.2.4 the pressure distribution along the flat plate is used as input for the COCO program 2.2.4 to generate velocity and temperature profiles and their respective spatial derivatives. These values are then the input for the linear local stability analysis conducted with LILO 2.2.4, which provides the envelopes of the amplification exponent, N. By intersecting the envelope curves with the transition positions measured with the infrared camera, the critical amplification exponents N_{crit} are obtained. More details on the procedure can be found in Sect. 2.2.4.

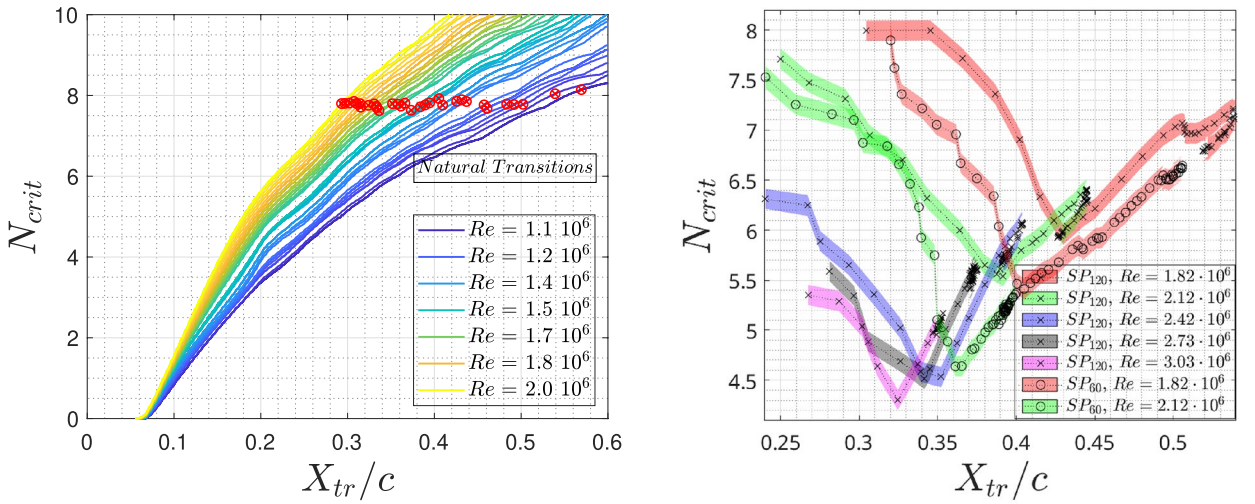

(a) Natural N_{crit} for different freestream velocities

(b) Comparison of N_{crit} for SP_{120} and SP_{60}.

Fig. 11 Critical amplification rates calculation, with/without boundary layer suction

The envelopes of N_{crit}, for the tested cases previously shown in Fig. 9, are presented for the natural transition of SP_{120} in Fig. 11a, exhibiting a rather constant behavior.

The same procedure is now applied to the transition location measured when varying the suction rate. Figure 11b compares the critical amplification factors between SP_{60} and SP_{120} as function of the transition location (X_{Tr}). The transition locations are the same as in Fig. 10; therefore, the measurement with a small X_{tr} corresponds to low-suction cases, and when c_Q increases the curve moves to the right side of the figure.

The SP_{120} surface, as observed before, starts approximately from the same N_{crit} value as c_Q=0, and displays always greater critical amplification exponents than SP_{60}, because the measured X_{tr} is higher for SP_{120} than for SP_{60} at fixed Re and c_Q. For both SP_{60} and SP_{120}, N_{crit} decreases in the region where c_Q and X_{tr} exhibit a linear relationship. Once N_{crit} reaches a minimum value, the curve begins to rise again for higher suction coefficient values.

For the highest value of c_Q, the behaviors of SP_{60} and SP_{120} differ. For SP_{120}, further increase of c_Q leads to the regression of the transition, and N_{crit} decreases accordingly. For SP_{60}, N_{crit} does not decrease but instead tends to cluster around a specific value, as the transition location remains mostly unchanged. Similar trends has been observed in Corelli Grappadelli et al. (2021) from tests performed at the MUB with the same flat plate geometry, and more recently by Helm et al. (2024) and Thamm and Scholz (2025) at the DNW-NWB with a different one, all resulting in a similar outcome.

The results indicate a different trend than previous interpretations of local linear stability theory, as in Mack (1977) and Van Ingen (2008), where at constant Re and freestream turbulence intensity, N_{crit} is expected to remain unchanged with varying c_Q.

From Fig. 11b, it can be inferred that each porous surface exhibits a distinct characteristic response and a specific deviation from the predictions of linear stability theory. This discrepancy may arise from the interaction between the boundary layer and multiple parameters affecting suction, including hole diameter, pattern, porosity, porous surface thickness, interacting turbulent vortices and sound amplification within the suction box (thus encompassing all design aspects of the suction system). In this study, only the hole diameter was modified, while all other parameters were kept the same, yet two different behaviors were observed. Hence, further studies should experimentally characterize the different parameters individually, aiming to extract new insights into their specific performance.

The effect of Re on the behavior of N_{crit} can be analyzed for the SP_{120} surface in Fig. 11b. The same trend previously discussed between X_{Tr} and N_{crit} is here observed. However, it is evident that as the Reynolds number increases, N_{crit} decreases significantly. Additionally, the curves no longer start at zero c_Q, which also contributes to this behavior. Nevertheless, it becomes clear that boundary layer suction is consistently less effective in our experiment than predicted by linear stability theory (LST).

Overall, these results indicate that the transition delay due to suction remains consistently lower than predicted by LST. The discrepancies between experimental data and numerical predictions can be categorized into three distinct regions for SP_{120} (two instead for SP_{60}):

1. In the first region, experimental data show a significant reduction in N_{crit}, indicating that transition location moves more slowly in the freestream direction under suction compared to LST predictions.
2. In the second region, transition advances more rapidly with increasing suction, partially recovering in terms of N_{crit}, yet remaining consistently lower than LST predictions.
3. In the third region, an excessively high suction coefficient introduces sufficient disturbances to induce a continuous upstream regression of the transition.

3.2 Boundary layer measurements

The effect of boundary layer suction on the flat plate is investigated through hot-wire measurements conducted on the suction panel, as introduced in Sect. 2.2.5. In Sect. 3.1, it has been shown that the transition location is moved further downstream by the suction panel with 120 µm diameter holes (SP_{120}) than by the panel with 60 µm diameter holes (SP_{60}). For this reason the SP_{120} is further studied here, and also because the SP_{120} surface exhibits another phenomena that is of interest, i.e., the regression of the transition line beyond a certain suction coefficient value.

The boundary layer measurements aim to identify the dominant cause-and-effect relationship responsible for the deviation in the N_{crit} (or the transition location) predicted by LST. It is important to note that the critical amplification factors were obtained by providing the pressure distribution and the coordinates of the flat plate as input. Consequently, the LST computation first determines the boundary layers over the entire surface before evaluating the critical amplification exponent. Any discrepancies will become evident within the boundary layers, particularly in the vicinity of the porous surface or further downstream.

The tests are conducted at a fixed $Re = 0.9 \times 10^6$ ($U_\infty = 15$ m/s) for several reasons. Primarily, the effects studied previously show rather little dependency on Reynolds number, allowing for the use of a lower Reynolds number to achieve a thicker boundary layer, facilitating more detailed measurements. As the disturbances originating from

the suction skin holes, remain close to the wall, it is challenging to measure them even at the reduced velocity of 15 m/s. At higher velocities, the experimental setup would likely fail to resolve such disturbances effectively. Moreover, operating at a lower freestream velocity significantly reduces the systematic error in hot-wire velocity calibration, as discussed in Sect. 2.2.5. Lastly, this lower velocity enables the experimental suction system to achieve higher suction coefficients with the available pump capacity.

3.2.1 Permeability effect

When boundary layer suction is not applied, two primary sources of disturbance to the laminar boundary layer, arising from the choice of porous surface typology, have been identified in the recent work of Rouviere et al. (2022): 1) impedance and 2) surface roughness. The boundary layer on the suction panel is measured with two configurations: one with the porous skin facing the flow and the other with the porous skin covered by a 50 µm thick layer of Kapton tape, placed on the outer side of the porous skin. In this way, it is possible to compare two configurations: one where both roughness and impedance are present without suction, and the other where only the external aerodynamics is considered, with no disturbances originating from the suction panel. The tape could introduce a disturbance by acting as a forward-facing step, however at the tested velocities the introduced step is subcritical, as explained in Sect. 2.3.

In Fig. 12a, the boundary layers measurements of the two different cases, with and without Kapton tape, are presented. These velocity profiles are obtained from the final measuring station on the porous surface $x/c = 0.22$, where the effect of permeability is expected to be the most pronounced. The boundary layers without tape exhibit a slightly lower shape factor, being approximately 0.1 lower, thus demonstrating the extent of the disturbance effect exerted by the permeability.

The velocity fluctuation $u'(z,t)$ is defined as the difference between the local mean velocity $\overline{U}(z)$ and the instantaneous velocity $U(z,t)$. Its overall magnitude is expressed as the root mean square of the streamwise and wall-normal components:

$$u'_{rms}(z,t) = |\overline{U}(z) - U(z,t)| = \sqrt{\langle u'^2(z,t)\rangle + \langle v'^2(z,t)\rangle}, \quad (3)$$

In Fig. 12b, velocity fluctuations for both configurations are presented, based on two datasets acquired at different times. With this setup, it is not possible to separate the effects of roughness and impedance. Nonetheless, near-wall differences of approximately 15% between the configurations with and without tape are observed.

It is concluded that the combined effect of impedance and surface roughness leads to an increase in the velocity fluctuations close to the wall and a reduction of the shape factor H_{12}. As will be demonstrated in Sect. 3.2.2, however, this disturbance is significantly lower than that induced while applying suction. Nevertheless, it remains an open question as to how much impedance can be amplified by suction Schrauf and Horstmann (2000), especially considering that, as shown by Rouviere et al. (2022), the effects of impedance were observed in the absence of suction.

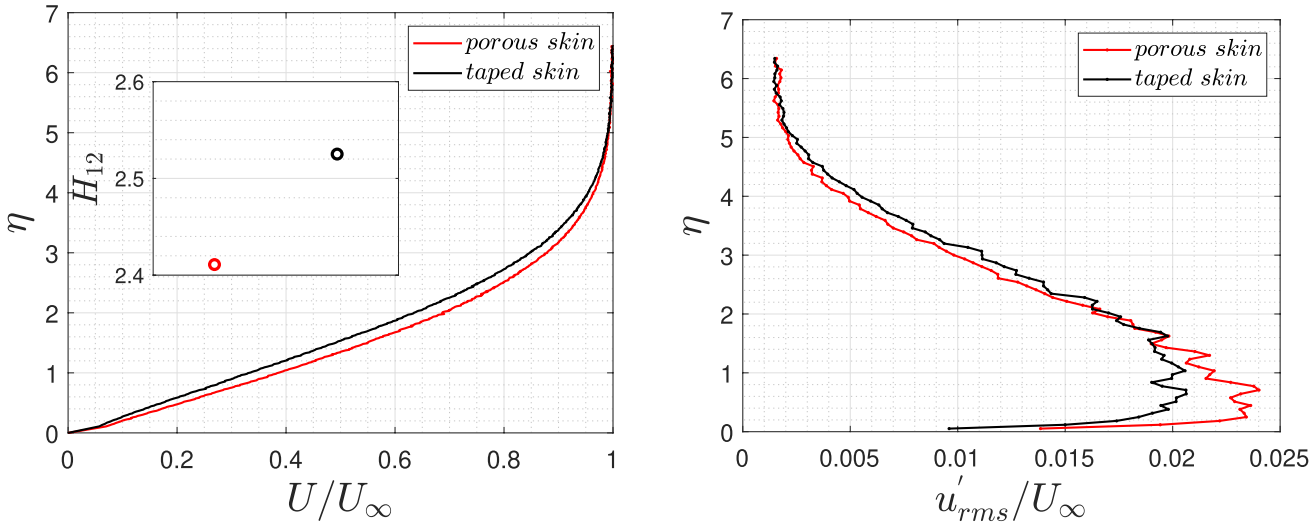

(a) Velocity profiles comparison.

(b) Velocity fluctuations comparison.

Fig. 12 Comparison of the velocity profiles for porous and solid wall, without suction, at $x/c = 22.2\%$

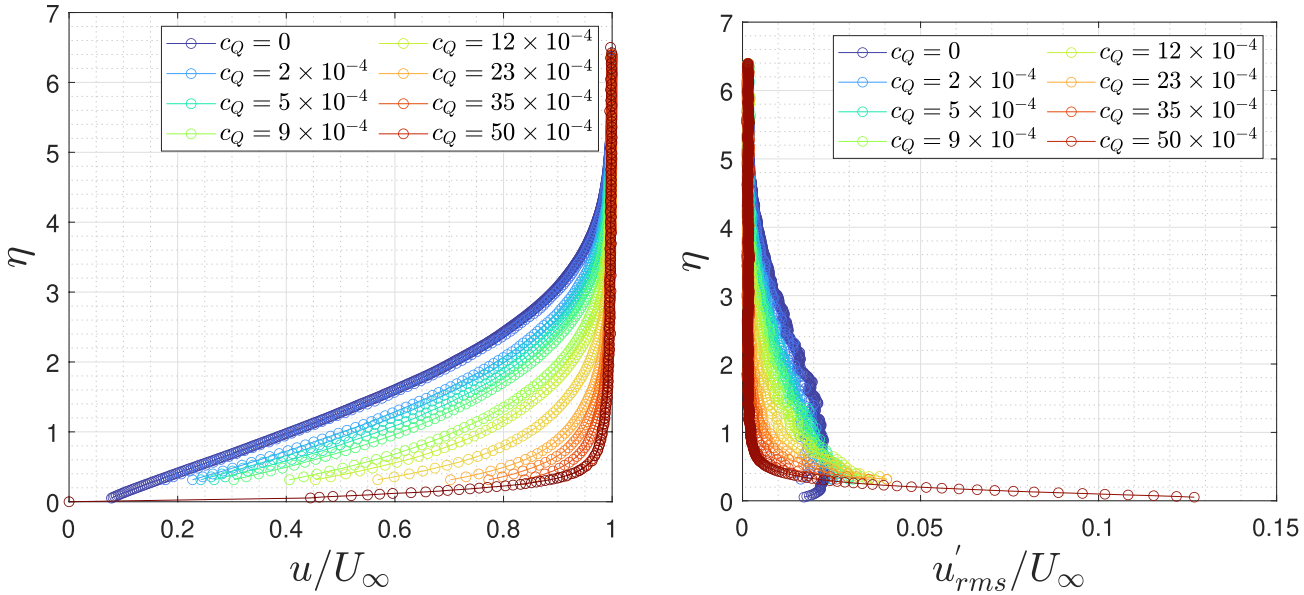

(a) One set of velocity profiles at x/c=22.2% for different suction rates.

(b) Velocity fluctuations.

Fig. 13 Boundary layer velocity profiles and velocity fluctuations at x/c=22.2%

3.2.2 Uniform suction

In this section, boundary layer suction is uniformly applied using all four suction chambers described in 2.1.2.

Figure13a displays the velocity distributions of the boundary layer at the last measurement point on the porous skin ($x/c = 0.22$), by varying the suction coefficient, c_Q. Wall suction exerts a stabilizing influence on the flow through two primary mechanisms. First, it diminishes the boundary layer thickness, second, it enhances the inherent stability of the streamwise velocity profile, thereby reducing the velocity fluctuations up to a certain suction velocity threshold (Schlichting and Gersten (2017), Macmanus and Eaton (2000)). In Fig. 13b, the root mean square of the velocity measurements is compared for the same velocity profiles of Fig. 13a. A consistent trend is observed in all subsequent results: as c_Q increases, fluctuations in the upper part of the boundary layer are dampened, highlighting the beneficial effects of suction in reducing the boundary layer thickness and velocity fluctuations. Conversely, the maximum fluctuation value increases, consistently occurring at the first measurement point on the porous skin.

Having established the influence of the c_Q on the boundary layer at the final measurement point along the porous surface, a second variable is introduced: the x-coordinate at which uniform suction is applied. The evolution of the amplitude functions is examined in Fig. 14 as a function of the suction coefficient c_Q and the normalized streamwise position x/c, based on measurements taken at twelve stations along the porous skin and four additional stations downstream, covering the range from $x/c = 0.15$ to 0.24 x/c. The Fourier amplitudes inside a laminar boundary layer of the u‘ and v’ disturbances in a flat-plate configuration is thoroughly described in Fasel and Konzelmann (2004). The peak closest to the wall is associated with the horizontal velocity component u, while the second peak, which is consistently of lower magnitude, corresponds to the vertical velocity component v. Equation (4) is used to compute the average amplitude $A(z)$ of the Fourier spectrum $|\hat{u}'(z,f)|$ within the frequency range characteristic of TS waves.

$$A(z) = \frac{1}{f_2 - f_1} \int_{f_1}^{f_2} |\hat{u}'(z,f)|\, df, \quad \text{with } f_1 = 190\,\text{Hz}, \quad f_2 = 230\,\text{Hz}. \tag{4}$$

Figure 14 presents the amplitude functions for increasing chordwise measurement points (for brevity, only a few of the most significant images are presented), determined as explained above and selected in the TS waves frequency range. A peak centered at 210 Hz was observed, extending from 190 Hz to 230 Hz. The LST for this flat plate geometry predicts that TS waves reach their maximum amplitude at a frequency of 250 Hz, so relatively close to the data. It is necessary to state that the amplitude of TS waves is very low because the measuring points are at the beginning of the boundary layer. Therefore, the objective is not to obtain a precise measurement of the eigenfunction of the TS waves but rather to assess the general effect of boundary layer suction at these early stages of the boundary layer.

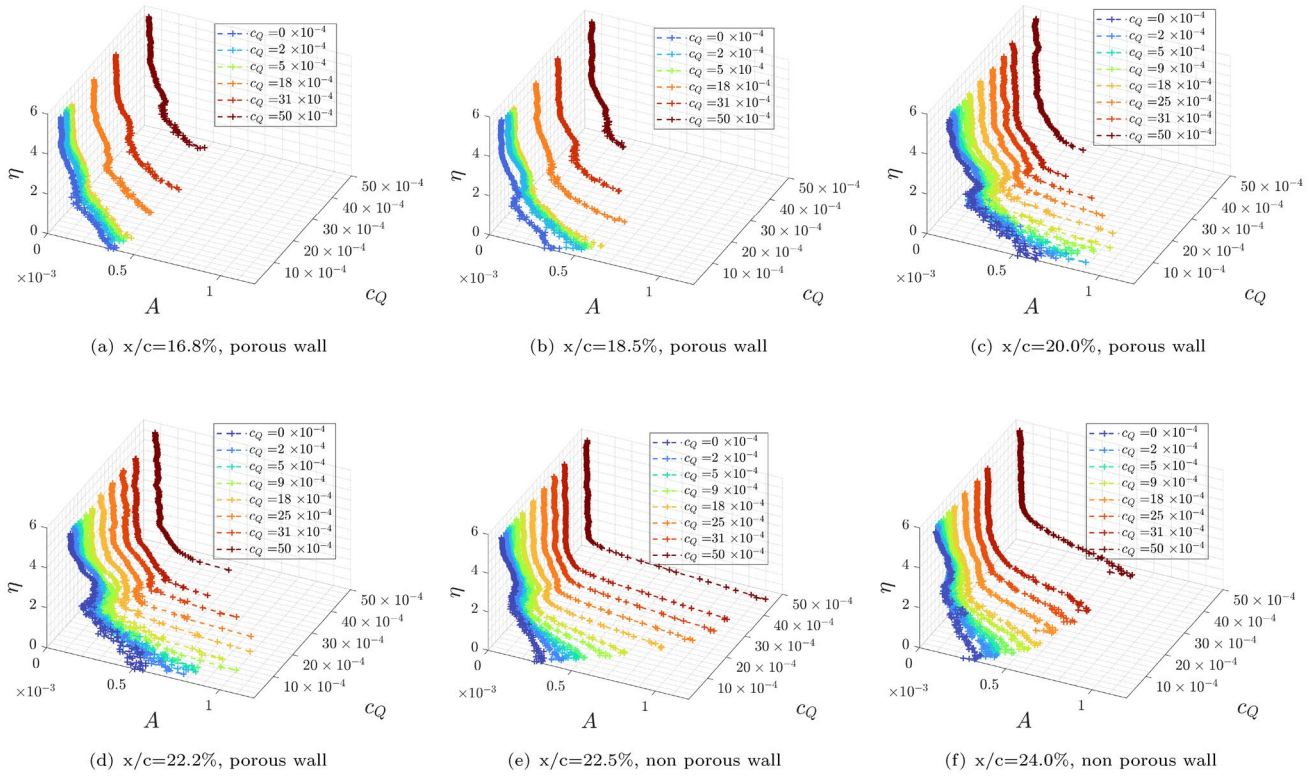

(a) x/c=16.8%, porous wall (b) x/c=18.5%, porous wall (c) x/c=20.0%, porous wall

(d) x/c=22.2%, porous wall (e) x/c=22.5%, non porous wall (f) x/c=24.0%, non porous wall

Fig. 14 Development of amplitude fluctuations caused by suction at increasing chordwise position

Measurement points from 14a–d are located on the suction box, while measurements in 14e–d are positioned on the wall following the suction panel.

Overall, the data presented in Fig. 14a–d indicate that the amplitude increases, reaching its maximum at the final measurement point just before the end of the suction box, while the boundary layer thickness significantly decreases with increasing suction and the chordwise position. As already discussed in relation to Fig. 13b, where a high-resolution measurement starting at 50 μm from the wall was included, the disturbance induced by the BLS shifts increasingly closer to the wall and becomes more intense as c_Q increases. In Fig. 14d, this high-resolution dataset taken at the same location is not included, as it would exceed the scaling used without providing additional insights. Nevertheless, this trend is still clearly evident from the first measurement point on the wall after the suction panel, where being no longer directly affected by BLS, the disturbances align sequentially, showing an orderly increase in disturbance intensity as a function of c_Q. Downstream of the porous skin (Fig. 14e–-d), the maximum amplitude occurs at the first wall measurement point for the highest c_Q, and progressively decreases from 1.2×10^{-3} at $x/c = 0.225$ to 0.6×10^{-3} at $x/c = 0.24$, indicating that the velocity fluctuations induced by boundary layer suction remain amplified only within the suction region. Regarding the measurements without suction, the amplitude values over the porous surface cases are larger than those observed on the solid surface, further confirming the destabilizing effect of impedance, combined with the roughness of the laser drilled panel, on boundary layer stability.

Figure15a displays the variation of the shape factor H_{12} as a function of both, the suction coefficient and the position along the x-axis for the 12 locations on the porous skin and the 4 positions beyond. The surface values were obtained by linear interpolation from the discrete data points indicated by black crosses. The minimum shape factor value is reached approximately at the midpoint of the suction box ($0.18x/c$, very close to the prediction of Iglisch and his theory for the asymptotic suction Iglisch (1944)) for the highest suction coefficient tested, after which the shape factor remains nearly constant, with a slight increase toward the end of the suction box. Downstream of the suction box, the shape factor exhibits a sharp increase. When comparing this trend with the shape factor computed by the boundary layer solver COCO in Fig. 15b, the corresponding difference is presented in Fig. 16. The numerical data were derived from the same experimental conditions, with additional points obtained by increasing the number of suction velocities; a linear interpolation was then applied to generate the surfaces illustrated.

The most significant discrepancy arises at the junction between the porous and solid walls. While the COCO

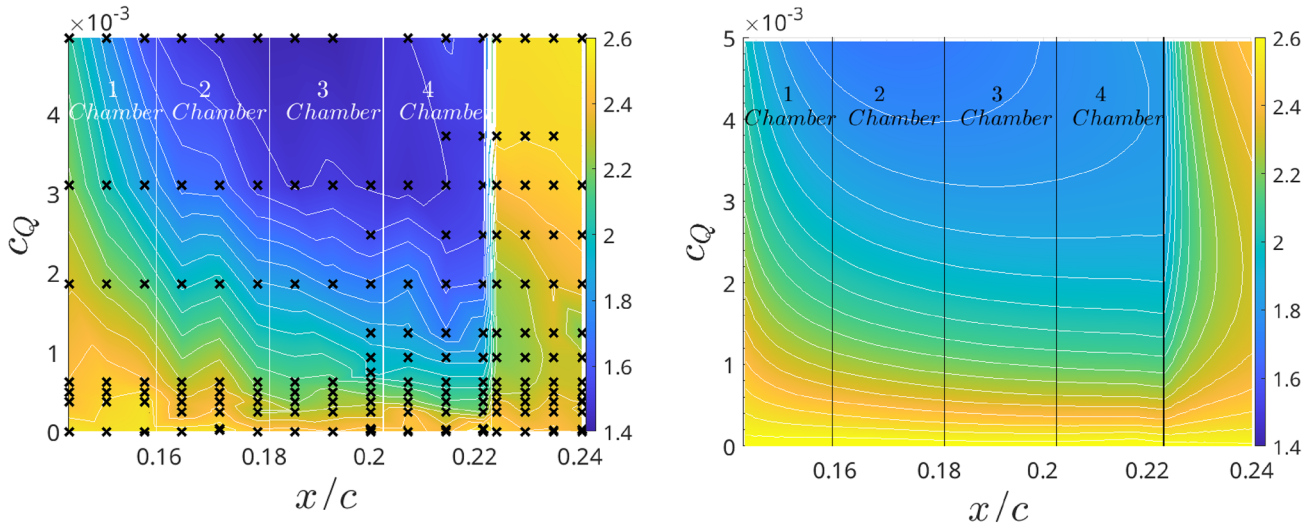

(a) Shape factor, Exp. measurements. (b) Shape factor, COCO.

Fig. 15 Shape factor H_{12} with homogeneous suction as a function of c_Q and of the chordwise position

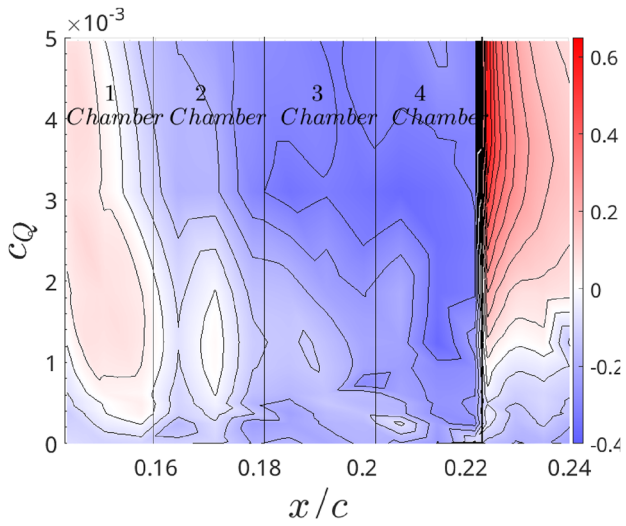

Fig. 16 Shape factor differences, Exp. data - COCO

solution predicts a gradual convergence to the value of 2.59, even for higher suction coefficients, the experimental data reveal a more pronounced discontinuity. This suggests that as suction increases, the modifications at the mean velocity profile introduced by suction cause the shape factor to deviate further from the values predicted by COCO. In particular, COCO tends to smooth out the transition between suctioned and non-suctioned wall sections. This is significant, as such a discontinuity may trigger secondary instabilities downstream of the suction panel or simply enhance the excitation of TS waves, in either case facilitating the early formation of turbulent spots and potentially shifting the transition closer to the leading edge.

Additionally, COCO predicts the minimum slightly earlier than the experimental data. Beyond this point, COCO predicts an increase in accordance with Iglisch (1944) and the asymptotic boundary layer, whereas the experimental data do not exhibit such a trend.

Consistent with the observations presented in this section and the discussion related to Figure 11b, the boundary layer solver COCO predicts a faster attainment of the minimum shape factor compared to what is observed in the experimental data. After reaching this minimum of H_{12}, the shape factor computed by COCO increases over the porous surface more than it does in the experimental data. It is concluded that the velocity fluctuations generated, regardless of the complex nature of the interactions between the vortices on the porous surface, appear to make the boundary layer fuller near the wall, while reducing the displacement thickness and increasing the velocity gradient at the wall relative to the numerical prediction.

In general, as previously anticipated, the vortical disturbances induced by the suction holes remain sufficiently weak to prevent significant inertial and pressure-driven instabilities, allowing the viscous effects to govern their dissipation. This is consistent with the observation that boundary layers over non-porous walls downstream of the suction surface gradually recover fluctuation amplitudes along the chord. However, it is evident that COCO, not accounting for such additional velocity fluctuations, predicts more stable boundary layers where turbulence occurs later than observed experimentally. The discrepancies observed in the boundary

layer meanflow could be resolved by using a higher-fidelity method for boundary layer prediction. Based on that it would be possible to measure the effect of the mean flow variation on the critical exponent N_{crit}.

The near-wall velocity fluctuations observed may influence the transition process itself; for instance, they could modify the onset of secondary instabilities and, consequently, alter the development of turbulent spots. This finding highlights the need for higher-fidelity simulations, such as direct numerical simulations (DNS), which are capable of resolving the later stages of transition with greater accuracy.

3.2.3 Discontinuous suction

In the current section, a discontinuous suction distribution is employed, where boundary layer suction is applied solely from the first and fourth chambers, effectively reducing the mass flow rate of suctioned air by half. The second and third chambers are covered with a 50 µm Kapton layer, effectively simulating a solid wall and removing the permeability effect. An additional measurement point located 2.95 m downstream of the leading edge, where the flow is turbulent for both configurations when BLS is not applied, showed that already at the lowest tested value of c_Q, both suction configurations produce a fully laminar flow at this Reynolds number, yielding nearly identical shape factors for the same suction coefficients.

In the continuous suction configuration, pronounced near-wall fluctuations were observed at the last four stations on the solid wall downstream of the porous section. In contrast, the application of discontinuous suction resulted in a marked reduction of near-wall fluctuations, as displayed in Fig. 17, which shows data from the first and last stations located on the solid wall section. Furthermore, the two peaks in the amplitude distribution within the boundary layer remain well separated in the discontinuous case, in contrast to the continuous configuration, where this separation disappears even at high suction coefficients.

Figure 18a presents the shape factor for this configuration, alongside the COCO prediction shown in Fig. 18b. The regions where boundary layer suction is applied are clearly distinguishable, with the minimum shape factor reached at the end of the fourth suction chamber, approaching a value of 1.4 for the highest suction coefficient.

This observation is particularly significant, as achieving the minimum shape factor at the end of the fourth chamber is consistent with the results obtained in the homogeneous case, where the minimum occurred near the end of the second chamber, also with a shape factor close to 1.4. This suggests that by maintaining a specific spacing between the suction surfaces, twice the size of the suction surfaces in this case, it is possible to replicate a flow behavior similar to that achieved with uniform suction over a larger surface area (in this case, twice as large). This finding highlights the potential for optimizing suction configurations to achieve laminarization over extended regions with zero pressure gradient while minimizing the required energy for actuating boundary layer suction by controlling the suction coefficient and its distribution along the chordwise direction. Minimizing the amount of sucked airflow while simultaneously reducing the disturbance introduced in the near-wall region of the boundary layer, yet still achieving its stabilization, emerges as a key finding of this experimental investigation.

Regarding the COCO predictions presented in Fig. 18b, they appear to be in better agreement than the ones for the continuous suction test case, as the discrepancies above

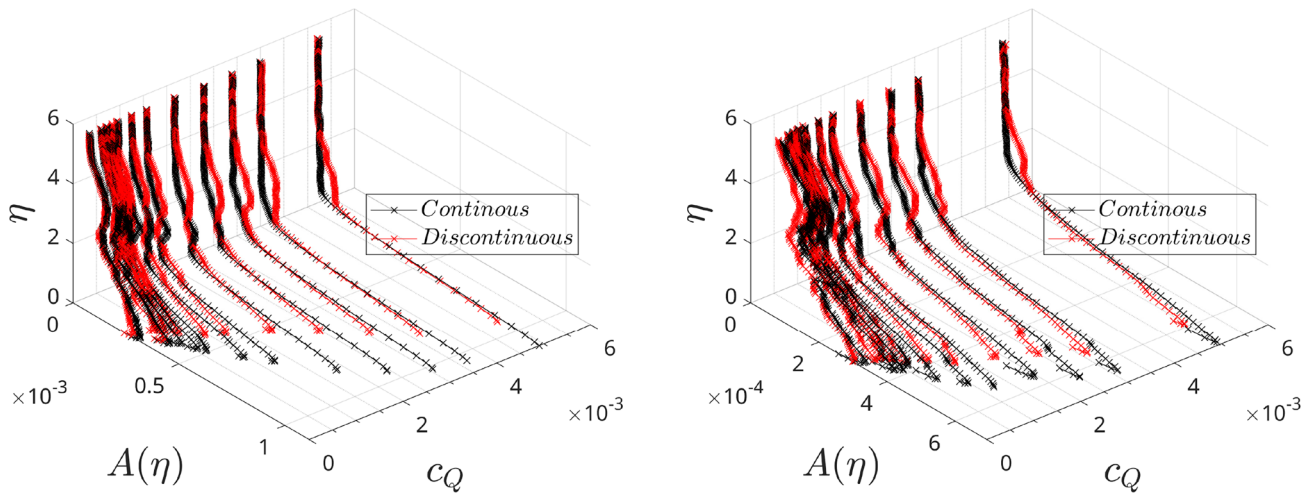

(a) $x/c = 0.225$. (b) $x/c = 0.240$.

Fig. 17 Comparison of the evolution of the amplitude functions for two different chordwise station after the porous skin

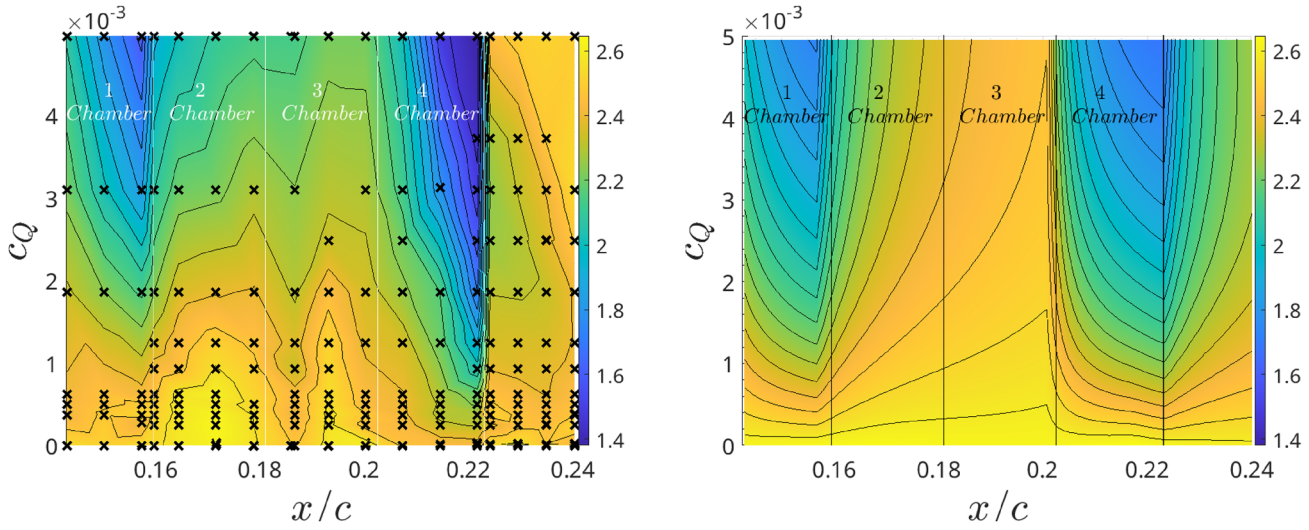

(a) Shape factor, Exp. data. (b) Shape factor, COCO.

Fig. 18 Shape factor H_{12} with discontinuous suction as a function of c_Q and of the chordwise position

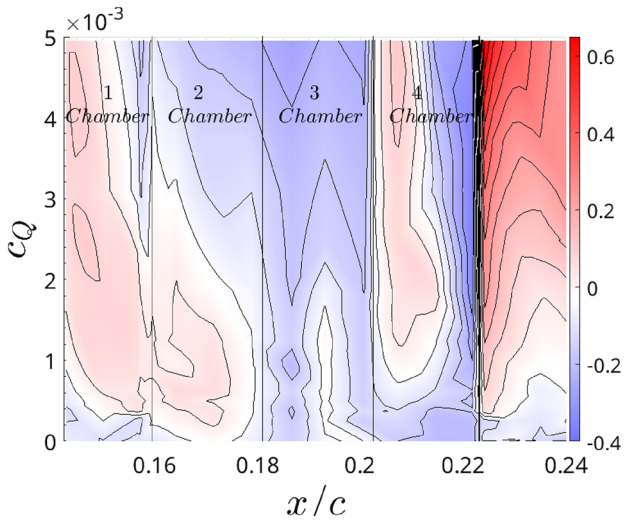

Fig. 19 Shape factor differences, Exp. data - COCO

the suction panel are significantly reduced, as reported in Fig. 19.

This further demonstrates that the extent of suction and its induced disturbance play a crucial role in the discrepancy between experimental data and numerical predictions. Downstream of the suction panel, the differences closely resemble those observed in the continuous case. Once again, COCO smooths out the transition to the solid wall and is less discontinuous than the experimental data in returning to higher values of shape factor. Once again, COCO yields a smoother recovery toward the solid wall and shows a less abrupt change than the experimental data in the return to higher shape factor values.

4 Conclusion

A wind tunnel experiment was conducted on a flat plate, with boundary layer suction between 14.5% and 22.5% of the chord length, featuring suction holes of 120 µm and 60 µm with 0.9% porosity. The experiments were conducted at various Reynolds numbers, with freestream velocities ranging from 15 m/s to 50 m/s. The suction coefficient c_Q, and its distribution along the chord were varied using four independently controlled suction chambers.

The results indicate that the transition location predicted by the traditional e^N approach, obtained via the numerical tool LILO, is systematically overestimated compared to experimental measurements as the suction coefficient increases. The discrepancy between LILO predictions and experimental data has been found to follow a consistent trend across all tested Reynolds numbers, determined by measuring the critical amplification exponent N_{crit}.

Specifically, at low-suction coefficient values, the deviation between the measured transition location and the LILO prediction initially increases, reaching a maximum. Beyond this point, corresponding to the minimum predicted N_{crit}, the discrepancy gradually decreases as the suction coefficient continues to rise, until a threshold is reached. Beyond this threshold, LILO predictions yield a constant N_{crit} value.

This final N_{crit} value remains lower than the one predicted without suction.

Only for the surface with 120 µm holes, a region of transition regression has been observed at very high suction coefficients tested and only for the lower Reynolds numbers tested. The surface with 120 µm diameter holes outperforms the surface with 60 µm holes in terms of transition control, though the observed gap diminishes as the Reynolds number increases.

Boundary layer measurements on the suction surface revealed disturbances, which manifested as a significant increase in near-wall velocity fluctuations. These fluctuations may influence the subsequent transition process, for instance by promoting the onset of secondary instabilities that lead to an earlier development of turbulent spots. In the discontinuity between the porous and solid wall, the experimental data exhibited a much sharper discontinuity, especially for the highest suction rates, whereas numerical predictions tended to smooth out the boundary layer values. The boundary layer measured in the experiments appears fuller and thinner than predictions from the boundary layer code COCO. These discrepancies in the mean flow profile, suggest that a higher-fidelity simulations (DNS) may be required to better assess the influence of the mean flow on the critical amplification exponent N_{crit}.

Trying to decouple the effect of suction distribution from the suction coefficient, a test case in which boundary layer suction was applied in a discontinuous manner through the first and last suction chambers was studied. In this discontinuous test case, the disturbance amplitude resulting from the interaction between suction and the boundary layer is lower, making it evident that the chordwise extent of the suction application plays a significant role in the amplification of the measured disturbance.

Acknowledgements We would like to acknowledge the funding by the Deutsche Forschungsgemeinschaft (DFG, German Research Foundation) under Germany's Excellence Strategy-EXC 2163/1-Sustainable and Energy Efficient Aviation-Project-ID 390881007. We would also like to thank Dr. Peter Scholz for his support with the graphite-heating surfaces and the analysis of disturbance amplitudes from boundary layer measurements and the Ing. Robert Schültzky for his dedication and effort during the wind tunnel tests.

Author contributions MCG contributed to the design of the wind tunnel model, setup of the measurement systems, execution of the experiments, post-processing of the experimental data, and writing of the manuscript. SA made contributions to model preparation, wind tunnel measurements and data processing, proof reading of the manuscript. RR assisted in the conceptual design of suction chambers, concept of presenting experimental data, proof reading of manuscript. CB contributed to the overall concept of wind tunnel experiment, supervision of measurements, concept of state of the art review, proof reading of manuscript. The first draft of the manuscript was written by MGC and all authors commented on previous versions of the manuscript. All authors read and approved the final manuscript.

Funding Open Access funding enabled and organized by Projekt DEAL.

Data availability The data presented in this work can be requested to MCG.

Declarations

Conflict of interest I declare that the authors have no Conflict of interest as defined by Springer, or other interests that might be perceived to influence the results and/or discussion reported in this paper.

Ethical approval Not applicable.

References

ASME (2006) Test uncertainty. Tech. rep., The American Society of Mechanical Engineers, American National Standard, https://www.asme.org/codes-standards/find-codes-standards/test-uncertainty

Beck N, Landa T, Seitz A et al (2018) Drag reduction by laminar flow control. Energies. https://doi.org/10.3390/en11010252

Bobbit P, Ferris CJ, D. HW, et al (1992) Results of the hybrid laminar flow control experiment conducted in the nasa langley 8-ft transonic pressure tunnel on a 7-ft chord model. NASA Tech Memorandum 19940028364 https://ntrs.nasa.gov/citations/19940028364

Braslow AL (1999) A history of suction-type laminar-flow control with emphasis on flight research. Monographs in Aerospace History, Number 13, NASA Technical Report 19990078750 https://ntrs.nasa.gov/citations/19990078750

Bruun H (1995) Hot wire anenometry, principles and signal analysis. Oxford Univ Press. https://doi.org/10.1093/oso/9780198563426.001.0001

Corelli Grappadelli M, Scholz P, Radespiel R, et al (2021) Experimental investigations of boundary layer transition on a flat plate with suction. In: AIAA SciTech conference, https://doi.org/10.2514/6.2021-1452

Corelli Grappadelli M, Sudhi A, Radespiel R et al (2022) Experimental study of a wing with hybrid laminar flow control application. AIAA Aviation Forum. https://doi.org/10.2514/6.2022-3770

Drela M (1989) Xfoil: An analysis and design system for low reynolds number airfoils. In: Conference on low reynolds number airfoil aerodynamics, University of Notre Dame, Mueller, T.J. (eds) Lecture notes in engineering, vol 54. Springer, Berlin, Heidelberg, pp 1–12, https://doi.org/10.1007/978-3-642-84010-4_1

Fasel H, Konzelmann U (2004) Non-parallel stability of a flat-plate boundary layer using the complete Navier–Stokes equations. J Fluid Mech. https://doi.org/10.1017/S0022112090003585

Fransson J, Alfredsson PH (2003) On the disturbance growth in an asymptotic suction boundary layer. J Fluid Mech 482:51–90. https://doi.org/10.1017/S0022112003003926

Gauffre G (1988) Detection of laminar-turbulent transition by infrared thermography. La Recherche Aerospatiale. https://doi.org/10.1007/s00348-016-2162-4

Goldsmith J (1957) Critical laminar suction parameters for suction into an isolated hole or a single row of holes. Northrop report BLC 95, NAI-57-529

Gregory N, Walker WS (1955) Experiments on the use of suction through perforated strips for maintaining laminar flow: transition and drag measurements. Aeronaut Res Council Rep Memoranda 3083 https://reports.aerade.cranfield.ac.uk/handle/1826.2/3653

Gregory N, Walker WS (1957) Wind tunnel tests on the use of distributed suction for maintaining laminar flow on a body of revolution. Aero Res Counc, Reports and memoranda 3145 https://reports.aerade.cranfield.ac.uk/handle/1826.2/3713

Hackenberg P, Rioual JL, Tutty OR et al (1995) The automatic control of boundary-layer transition—experiments and computation. Appl Sci Res 54:293–311. https://doi.org/10.1007/BF00863515

Hefner JH, Sabo FE (1987) Research in natural laminar flow and laminar-flow control. NASA conference publication 2487 https://ntrs.nasa.gov/citations/19900003187

Heintz A, Scholz P (2023) Measurements on the effect of steps on the transition of laminar boundary layers. Exp Fluids. https://doi.org/10.1007/s00348-023-03614-x

Helm S, Grabe C, Krumbein A, et al (2024) Wind tunnel test with boundary layer suction for the validation of transition transport models. In: AIAA Scitech conference, https://doi.org/10.2514/6.2024-2686

Iglisch R (1944) Exact calculation of laminar boundary layer in longitudinal flow over a flat plate with homeogeneous suction. Tech. rep., National advisory committee for aeronautics, NACA Technical Memorandum 20050019547, https://ntrs.nasa.gov/citations/20050019547

Joslin RD (1998) Overview of laminar flow control. NASA technical report https://ntrs.nasa.gov/citations/19980232017

Mack LM (1977) Transition and laminar instability. 38th fluid dynamics conference and exhibit pp 77–15. https://ntrs.nasa.gov/citations/19770017114

Macmanus DG, Eaton JA (1996) Predictions and observations of the flow field induced by laminar flow control microperforations. Exp Thermal Fluid Sci. https://doi.org/10.1016/S0894-1777(96)00094-5

MacManus DG, Eaton JA (1998) Measurement and analysis of the flowfields induced by suction perforations. AIAA J 10(2514/2):563

Macmanus DG, Eaton JA (2000) Flow physics of discrete boundary layer suction—measurements and predictions. J Fluid Mech 417:47–75. https://doi.org/10.1017/S0022112000001026

Messing R, Kloker MJ (2010) Investigation of suction for laminar flow control of three-dimensional boundary layers. J Fluid Mech 658:117–147. https://doi.org/10.1017/S0022112010001576

Methel J, Forte M, Vermeerschl O et al (2015) An experimental study on the effects of two-dimensional positive surface defects on the laminar-turbulent transition of a sucked boundary layer. Exp Fluids. https://doi.org/10.1007/s00348-019-2741-2

Nenni JP, Gluyas GL (1966) Aerodynamic design and analysis on an LFC surface. Astronaut Aeronaut 4(7):52–57

Petzold R (2014) Untersuchungen zum einfluss spannweitig stark veränderlicher strömung auf den laminar turbulenten grenzschichtumschlag. PhD thesis, Institut für Strömungsmechanik, TU Braunschweig

Petzold R, Radespiel R (2015) Transition on a wing with spanwise varying crossflow and linear stability analysis. AIAA Journal. https://doi.org/10.2514/1.J053127

Pfenninger W (1946) Untersuchungen über reibungsverminderungen an tragflugeln, insbesondere mit hilfe von grenzschlichtabsaugung. PhD thesis, ETH Zürich

Pfenninger W (1977) Laminar flow control laminarization. AGARD Report No654, Special Course on Concepts for Drag Reduction

Pfenninger W, Syberg J (1974) Reduction of acoustic disturbances in the test section of supersonic wind tunnels by laminarizing their nozzle and test section wall boundary layers by means of suction. Contractor Report 19750004905 https://ntrs.nasa.gov/citations/19750004905

Prasannakumar A, Wolff J, Radespiel R et al (2022) Design and power calculation of HLFC suction system for a subsonic short-range aircraft. CEAS Aeronaut J 13:1003–1026. https://doi.org/10.1007/s13272-022-00614-1

Reed HL, Nayfeht AH (1982) Numerical-perturbation technique for stability of flat-plate boundary layers with suction. AIAA Journal. https://doi.org/10.2514/3.9247

Reynolds GA, Saric WS (1985) Experiments on the stability of the flat-plate boundary layer with suction. AIAA J 24(2). https://doi.org/10.2514/3.9246

Rouviere A, Méry F, Methel J, et al (2022) Experimental and numerical study on wall impedance effects on tollmien–schlichting waves. AIAA Journal. https://doi.org/10.2514/1.J060536

Schlichting H, Gersten K (2017) Boundary-layer theory. Springer Berlin Heidelberg. https://doi.org/10.1007/978-3-662-52919-5

Schrauf G (1998) Coco-a program to compute velocity and temperature profiles for local and nonlocal stability analysis of compressible, conical boundary layers with suction. Tech. rep, ZARM Technical Report

Schrauf G (2006) Lilo 2.1 - user's guide and tutorial. Tech. Rep. 6, GSSC Technical Report

Schrauf G (2015) Large-scale laminar-flow tests evaluated with linear stability theory. J Aircraft. https://doi.org/10.2514/1.9280

Schrauf G, Horstmann H (2000) Linear stability theory applied to natural and hybrid laminar flow experiments. In: DGLR-Fachsymposium AG STAB, Stuttgart, Germany, pp 157–163, https://doi.org/10.1007/978-3-540-45359-8_17

Simon B, Schnabel P, Grundmann S (2016) Ir measurements for quantification of laminar boundary layer stabilization with DBD plasma actuators. Springer International Publishing Switzerland 132:269–278. https://doi.org/10.1007/978-3-319-27279-5_24

Squire HB (1933) On the stability for three-dimensional disturbances of viscous fluid flow between parallel walls. R Soc. https://doi.org/10.1098/rspa.1933.0193

Sudhi A, Elham A, Badrya C (2021) Coupled boundary-layer suction and airfoil optimization for hybrid laminar flow control. AIAA J 59(12):1–16. https://doi.org/10.2514/1.J060480

Thamm K, Scholz P (2025) Experimental study of boundary layers under the influence of multiple suction surfaces on a HLFC-capable flat plate. AIAA SciTech Conf. https://doi.org/10.2514/6.2025-0263

Tilton N, Cortelezzi L (2015) Stability of boundary layers over porous walls with suction. AIAA Journal. https://doi.org/10.2514/1.J053716

Van Ingen J (2008) The e^n method for transition prediction: historical review of work at TU Delft. 38th Fluid dynamics conference and exhibit https://doi.org/10.2514/6.2008-3830

Von Soldenhoff R, Lüdeke H (2024) Interaction of boundary layer and suction chamber of a laminarization system. AIAA Journal, Volume 63, Number 4 https://doi.org/10.2514/1.J064184

Zhao L, Dong M (2020) Effect of suction on laminar-flow control in subsonic boundary layers with forward-/backward-facing steps. Phys Fluids 32:054108. https://doi.org/10.1063/5.0007624